A High Precision and High Efficiency PMSM Driver Based on Power Amplifiers and RTSPSs

Xiaofeng Ding, *Member, IEEE*, Jiawei Cheng, Zhihui Zhao, Partrick Chi kwong Luk, *Senior Member, IEEE*

Abstract- **A novel topology based on linear power amplifiers (PAs) and real-time sinusoidal voltage-adjustment power supply systems (RTSPSs) for a permanent magnet synchronous motor (PMSM) drive system is proposed in this paper. Here, PAs are applied to achieve high-precision motor drive control and minimize the motor torque ripple and harmonic loss caused by nonlinearities of the inverter in traditional space vector pulse-width modulation. Meanwhile, in order to improve the conversion efficiency of PAs, the traditional DC power supply system of PAs is replaced by the RTSPSs, which is based on the wide-band-gap devices. The experimental results show that the efficiency of PAs in the motor system is increased from 58.88% to 79.25%, and the fluctuation of the motor speed at a given speed of 2rpm is reduced from 27rpm to 0.5rpm.**
Index Terms—linear power amplifiers, real-time sinusoidal voltage-adjustment power supply systems, permanent magnet synchronous motor, wide-band-gap devices

I. INTRODUCTION

Permanent magnet synchronous motor （PMSM） is widely used in aerospace and military industry due to its high-power density, wide speed range, and flexible control. There are a couple of methods that can be applied to achieve high-precision control of PMSM such as include space vector pulse-width modulation (SVPWM) and linear power amplifiers (PAs). The traditional SVPWM method is easy to realize for a full digital control with small losses. However, the output current distortion caused by non-linear factors of the inverter such as switching device voltage drop and dead time, which will induce torque ripple and harmonic loss in the motors[1-2]. Additionally, the high-frequency modulation switching action of devices may cause an over-voltage in the transmission cable and damage its insulation, resulting in huge shaft current in the motor and shortening service life of the motor [2].

Recently, in order to reduce current harmonics caused by the SVPWM controller and improve the control accuracy of the motor, many methods such as approximate dead-time-free PWM modulation and pulse width compensation are proposed [3-7]. The approximate dead-time-free PWM modulation method omits the unnecessary turning on or off of the power

This paper is an extension of "A Real-time Sinusoidal Voltage-Adjustment Power Supply Based on Wide-Band-Gap Devices for Linear Power Amplifier", 2019 IEEE Energy Conversion Congress and Exposition.

X. Ding, J. Cheng and Z. Zhao with the School of Automation and Electrical Engineering, Beihang University, Beijing, China. (Email: dingxiaofeng@buaa.edu.cn, chengjiawei0218@126.com, zzh18254989870 @ 126.com)

P.C.K. Luk is with the Power Engineering Centre, Cranfield University,Cranfield MK43 0AL, U.K. (e-mail: p.c.k.luk@cranfield.ac.uk).
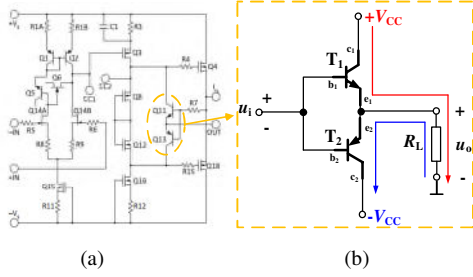
device to reduce the non-linear effects caused by the dead time [5]. In [6] and [7], the pulse width compensation method is proposed to compensate the current distortion caused by the dead zone effect. This method adjusts the duty cycle of the PWM signal by deriving the relationship between the output voltage error of the inverter and the polarity of the motor phase current. A disturbance observer was designed to observe and compensate the inverter output non-linear error in the motor drive system [8].

Although the aforementioned studies offer methods for the compensation of the dead-time effects and voltage drop of the inverter, none of the proposed methods can eliminate the non-linearity effects. Thanks to the Linear power amplifiers （PAs）, which can provide a pure sinusoidal output voltage, should be a best choice to achieve the further accuracy improvement. This method can avoid a series of problems caused by current harmonics, such as the torque ripples and additional losses of motors. Meanwhile, PA drive system is also friendlier to the motor due to the effective avoidance of the overvoltage and high shaft current which is induced by steep edges of the PWM [9].

At present, integrated linear PAs are mostly used for motors driven by H-bridges, such as brushed DC motors, two-phase stepper motors, and voice coil motors. In [10] a PA module OPA2541 was used to output a PWM waveform to drive the motor. This control method can obtain higher control accuracy through a simple circuit structure. However, it is only suitable for single-phase motors and no consideration is given to minimize the abundant losses of the PA. Hence, the efficiency of the system is low. In [11], an integrated PA module TDA1521 was used to drive a stepper motor produced by MI TSUMI in Japan. Experiment results showed that the current ripple of the motor is small, and the two-phase stepper motor obtains a high-precision position control. However, the power level of the drive system is small, and the PA generates a considerable amount of heat. After comparing the advantages and disadvantages of several types of PAs, Carsten Wallenhauer and others studied drivers based on Class B PAs for piezo actuator drives (PAD) [12]. They established a loss model of the PA and proposed a method through switching the power supply of the power transistor with an external capacitor to reduce the voltage drop on the transistor, thus reducing the losses of PAs. However, this method is only suitable for capacitive loads, and the efficiency is improved by sacrificing the linearity of the PA output voltage.

Although linear PAs can be applied to obtain a high control accuracy, severe heat generation limits the power level and reduces the power density of motor drive systems. At present,

(a) (b)

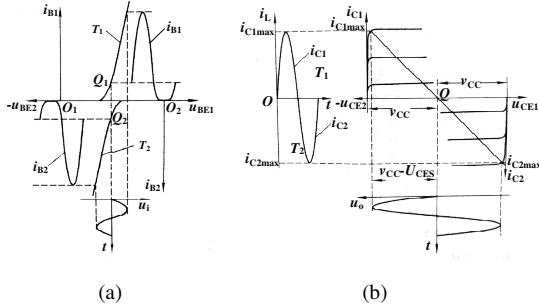Fig. 1. OCL power amplifier circuit. (a) Internal structure. (b) Simplified structure.

(a) (b)

Fig. 2. Working principle of the OCL. (a) The input features of the T_1 and T_2 transistors under u_i. (b) The waveform analysis diagram of the OCL power amplifier circuit.

most research studies about the efficiency improvement of PA focus on the radio frequency power amplifier (RFPA), such as switching RFPA technology, envelope elimination and restoration (EER) [13], linear amplification with nonlinear component (LINC) [14], and envelope tracking (ET) technology. Utilizing ET technology, the supply voltage on the transistors of Class A and Class B amplifiers can be adjusted dynamically according to the input signal to improve the efficiency of the PAs, while the high linearity is also maintained.

There are two circuit structures to achieve the ET supply voltage: a DC converter and a DC converter combined with a linear unit. In [15] and [16], multilevel technology was applied to realize the envelope tracker. The output voltage of the envelope tracker can only be converted between several fixed voltage values based on the reference signal. As the number of fixed voltages increases, the efficiency of the power amplifier increases, nevertheless, the voltage distortion intensifies . In [17], ET technology was implemented by means of a DC converter combined with a linear unit. This method is based on a hysteresis current control and the efficiency is increased to 60%.

Different from PAs used in a motor drive system, the fundamental frequency of the RFPA is up to MHz and the fundamental waveform is unipolar. Meanwhile, ET technology with incomplete envelope supply voltage can meet the efficiency requirements of the PA under conditions of low power and high frequency.

In summary, there is little research on the application of PAs for motor drives, especially for PMSM. Meanwhile, a solution with high precision, strong applicability and

significant efficiency improvement has not been reported in the field of motor drives.

Thanks to the emerging wide-band-gap power devices with high switching frequency operation and relatively low switching losses, it provides favorable conditions for solving the serious loss of PAs in motor systems. Therefore, this paper proposes a novel PMSM drive topology based on PAs and a real-time sinusoidal voltage-adjustment power supply systems (RTSPS) for PAs [18]. While achieving high-precision motor control, it also greatly improves the efficiency of the PAs and realizes a motor-friendly drive system with high accuracy, low torque ripple and high efficiency.

II. A REAL-TIME SINUSOIDAL VOLTAGE-ADJUSTMENT POWER SUPPLY SYSTEM

A. Loss model of PA under traditional power supply mode

Taking the output capacitorless (OCL) power amplifier circuit shown in Fig. 1 as an example, the NPN transistor T_1 and the PNP transistor T_2 have symmetrical features and are powered by a $\pm V_{CC}$ dual-power supply.

The input features of the T_1 and T_2 transistors under u_i are shown in Fig. 2(a). The waveform analysis diagram of the OCL power amplifier circuit is shown in Fig. 2(b).

When $u_i = 0V$, then $u_{b1} = u_{b2} = 0V$ and both T_1 and T_2 are cut off, hence, the output voltage $u_o = 0V$. When u_i is a sinusoidal signal and $u_i > 0V$, then $u_{c1} > u_{b1} > u_{e1}$, T_1 is turned on and operates in the amplification area while T_2 is turned off, then the $+V_{CC}$ supplies power to the load. When $u_i < 0V$, then $u_{e2} > u_{b2} > u_{c2}$, T_2 is turned on and operates in the amplification area while T_1 is turned off, hence $-V_{CC}$ supplies power to the load. The two transistors are in a complementary working mode.

According to Fig. 2(b), the static operating point Q is set on the horizontal axis due to the complementary operation mode of the transistors, namely $i_C=0$. Hence, the cut off-distortion does not occur. In order to avoid saturation distortion of the PA output voltage, it must be guaranteed that

$$u_{CE} = V_{CC} - u_o = V_{CC} - U_{om} \sin(\omega t) \geq u_{CES} \qquad (1)$$

where, V_{CC} is the supply voltage for PA, U_{om} is the maximum undistorted output voltage of the amplifier, and u_{CES} is the saturation voltage drop of the transistor. Then,

$$U_{om} \leq V_{CC} - u_{CES} \qquad (2)$$

It is known from (2) that for the OCL power amplifier circuit, as long as the maximum output voltage of the power amplifier does not exceed the difference between the power supply voltage and the saturation voltage drop, the saturation distortion of PA output voltage can be avoided.

The loss of a PA is mainly caused by the voltage drop between the collector and the emitter of the transistor and the current flowing through the transistor, that is

$$P_{loss} = u_{CE} \cdot i_C \qquad (3)$$

where, u_{CE} is the voltage drop across the transistor, and i_C is the current flowing through the transistor. The traditional DC
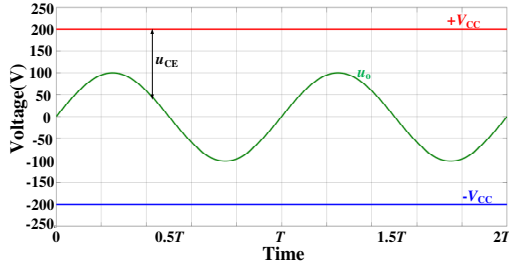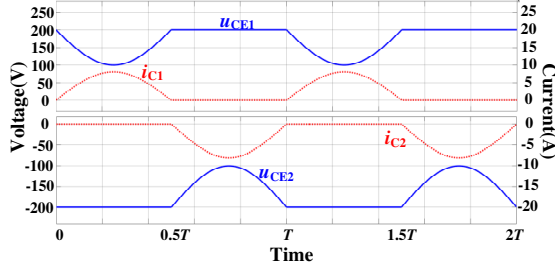
Fig. 3. Normal DC power supply and output voltage waveform.

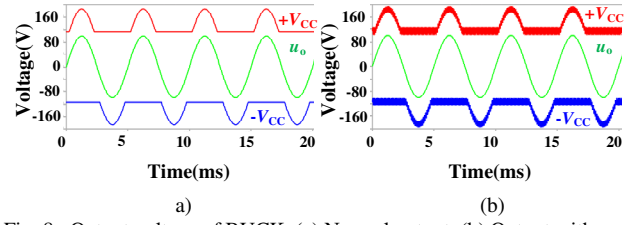Fig. 4. The voltage and current waveforms on T_1 and T_2 under the Normal power supply mode.

Fig. 8. Output voltage of BUCK. (a) Normal output. (b) Output with harmonics.
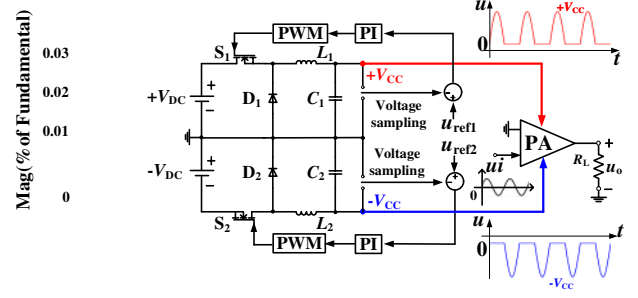
Fig. 9. FFT harmonics.
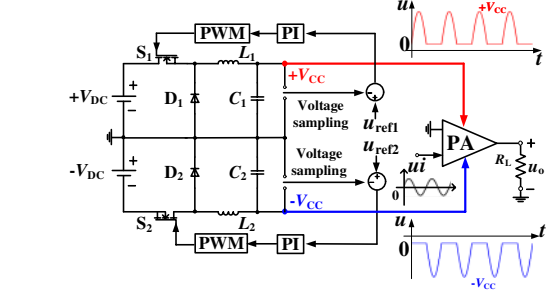
Fig. 10. Circuit structure of the proposed RTSPSs.
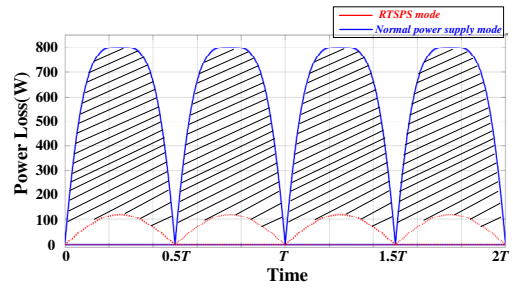
power supply mode is shown in Fig. 3, while the voltage and current on T_1 and T_2 are shown in Fig. 4.

When the output voltage of the PA is $u_o = u_{om}\sin(\omega t)$, the average output power P_o, input power P_{in} and conversion efficiency η of the PA can be calculated under the traditional DC power supply mode,

$$P_o = \frac{1}{\pi}\int_0^\pi \frac{\left(U_{om}\sin(\omega t)\right)^2}{R_L}d\omega t = \frac{U_{om}^2}{2R_L} \tag{4}$$

$$P_{in} = \frac{1}{\pi}\int_0^\pi \frac{U_{om}\sin(\omega t)}{R_L}\cdot V_{CC}d\omega t = \frac{2U_{om}V_{CC}}{\pi R_L} \tag{5}$$

$$\eta = \frac{P_o}{P_{in}} = \frac{\pi U_{om}}{4V_{CC}} \le \frac{\pi\left(V_{CC}-u_{CES}\right)}{4V_{CC}} \tag{6}$$

Ideally, the transistor voltage drop of the transistor U_{CES} is assumed as 0, the maximum conversion efficiency of the PA is about 78.5%, and the average efficiency in an actual application is less than 50%.

B. Loss model of PA under RTSPSs mode

In order to reduce the power losses when the PA works, RTSPSs was proposed in our previous work [18]. The RTSPSs power supply mode is shown in Fig. 5, while the voltage and current on T_1 and T_2 are shown in Fig. 6 respectively. Under the same working conditions, the output power, average input power and conversion efficiency of the PA in RTSPSs are

$$P_o' = P_o = \frac{1}{\pi}\int_0^\pi \frac{\left(U_{om}\sin(\omega t)\right)^2}{R_L}d\omega t = \frac{U_{om}^2}{2R_L} \tag{7}$$

$$P_{in}' = \frac{1}{\pi}\int_0^\pi \frac{U_{om}\sin(\omega t)}{R_L}\cdot\left(u_{CES}+U_{om}\sin(\omega t)\right)d\omega t$$

Fig. 7. Losses comparison of PA between two modes.

$$= \frac{2U_{om}u_{CES}}{\pi R_L} + \frac{U_{om}^2}{2R_L} \tag{8}$$

$$\eta' = \frac{P_o'}{P_{in}'} = \frac{1}{\dfrac{4}{\pi}\cdot\dfrac{u_{CES}}{U_{om}}+1} \tag{9}$$

Ideally, the voltage drop of the transistor U_{CE} is assumed as 0, and the efficiency of the PA can achieve 100%.

As shown in Fig. 7, the power losses of PA in the proposed RTSPSs mode is significantly reduced compared with the traditional mode.

In this paper, PAs supply power for the motor, while the BUCK converters supply $\pm V_{CC}$ for PAs, RTSPS and PA93 are two different systems. According to the structure of RTSPS, V_{CC} is generated by the BUCK converter, the action of the switch inevitably creates harmonics on the V_{CC}, but according to the Eq.(2), as long as the U_{om} is guaranteed not to exceed the difference between V_{CC} and u_{CES}, the output of PA93 can avoid saturation distortion.

We carry out real-time power supply superimposed with high frequency harmonics for the PA93 and compared with the case without superimposed harmonics. As shown in Fig. 8,

$\pm V_{\text{CC}}$ is generated by the RTSPS and the u_{o} is outputted by the PA93. Fig. 9 shows that the total harmonic distortion(THD) is 0.062% and 0.065% respectively. Fig. 9 confirms that the fluctuates on $\pm V_{\text{CC}}$ have tiny influence on the u_{o} when the Eq(3) is satisfied.

C. Circuit topology and simulation of the RTSPSs

Based on the above theoretical analysis, a bipolar BUCK circuit was proposed to realize the RTSPSs for the PA. The circuit topology is shown in Fig. 10, which can adjust the output voltage according to the need.

When $u_{\text{i}}>0$, the positive BUCK circuit provides $+V_{\text{CC}}$. When $u_{\text{i}}<0$, the negative BUCK circuit provides $-V_{\text{CC}}$. The relationship between the input voltage u_{i} of the PA and the given voltage u_{ref} of the BUCK circuit is shown as follows,

$$\begin{cases} u_{\text{ref1}} = A \cdot u_{\text{i}} + u_{\text{CES}}, u_{\text{i}} \geq 0 \\ u_{\text{ref2}} = A \cdot u_{\text{i}} - u_{\text{CES}}, u_{\text{i}} < 0 \end{cases} \quad (10)$$

where, A is the voltage amplification factor of the linear power amplifier.

The transfer function of BUCK converter is a second-order system and we choose PI regulator to improve the performance of the system. From the Bode diagram, we can calculate that P=0.141，I=6709. Due to the error between the actual system parameters and the theoretical value, the PI parameters of the actual system need to be adjusted appropriately. Finally, the PI control parameters are P=0.1 and I=5000.

The main factors restricting the selection of inductance and capacitance parameters in BUCK converter are the ripples of output current and voltage. According to the inductance characteristic equation,

TABLE I
SIMULATION PARAMETERS

Switching frequency	Inductance		Capacitance		Resistance
	Value	Weight	Value	Weight	
15kHz	500μH	59g	27μF	31.4g	20Ω
100 kHz	100μH	20.4g	4.7μF	10.2g	20Ω

$$(u_{\text{in}} - u_{\text{o}}) = L\frac{\Delta I}{t_{\text{on}}} \quad (11)$$

we obtain the expression of the inductance parameter by the follow equation,

$$L = \frac{t_{\text{on}}(u_{\text{in}} - u_{\text{o}})}{\Delta I} = \frac{(u_{\text{in}} - u_{\text{o}})}{\Delta I}\frac{u_{\text{o}}}{u_{\text{in}}}T \quad (12)$$

where, t_{on} is the turn-on time of the MOSFET, ΔI is the ripple of inductive current, u_{in} and u_{o} are the input and output voltage of the BUCK circuit respectively, and T is the switching period of the MOSFET. According to the requirements, $\Delta I_{\text{max}}=5\text{A}$, $u_{\text{in}}=200\text{V}$, when $u_{\text{o}}=100\text{V}$, the ripple reaches its maximum, if the inductance can effectively suppress the current ripple in this case, it can also ensure the normal operation of the circuit when the output voltage is smaller than 100V. Hence, we obtain $L=100\mu\text{H}$.

There is an integral relation between voltage ripple and current ripple.

$$\Delta u = \frac{1}{C_{\text{o}}}\int_{0}^{0.5T} i\, dt = \frac{1}{C_{\text{o}}} \times \frac{1}{2} \times \frac{T}{2} \times \frac{\Delta I}{2} \quad (13)$$
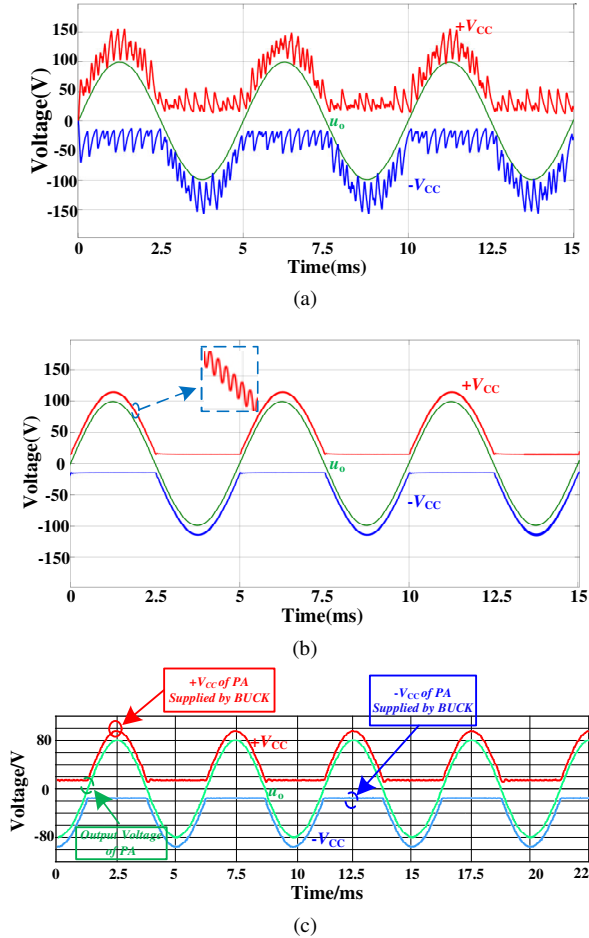
Fig. 11. Output of RTSPSs. (a) f_s=15kHz. (b) f_s=100kHz. (c) The experimental waveforms: f_s=100kHz

Fig. 12. Comparison of RTSPSs simulation. (a) f_s=15kHz. (b) f_s=100kHz. (c) The experimental waveforms: f_s=100kHz

According to the requirements, ΔU_{max}=1.33V, we can figure out that C_o=4.7μF.

In addition to the inductance and capacitance, switching frequency also affects the output ripple of the BUCK converter. Compared with the 15 kHz switching frequency in Fig. 11(a), the harmonics are significantly reduced when the switching frequency increases to 100 kHz as is shown in Fig. 11(b), the values of inductance and capacitance are reduced to 20% while the total weight is reduced to 30% as shown in Table I. The experimental waveform corresponding to Fig. 11(b) is Fig. 11(c).

The dynamic performance of BUCK converter can be improved obviously because the high switching frequency can reduce the value of inductance and capacitance. As shown in Fig. 12(a) and (b), when the switching frequency is 15kHz and the fundamental wave frequency is 500Hz, the lag time is 450μs, while the lag time is 80μs when the switching frequency is 100kHz and the fundamental wave frequency is 1kHz . The experimental waveform corresponding to Fig. 12(b) is Fig. 12(c). Therefore, the high switching frequency plays an important role in reducing the volume of the system and improving the dynamic response performance.
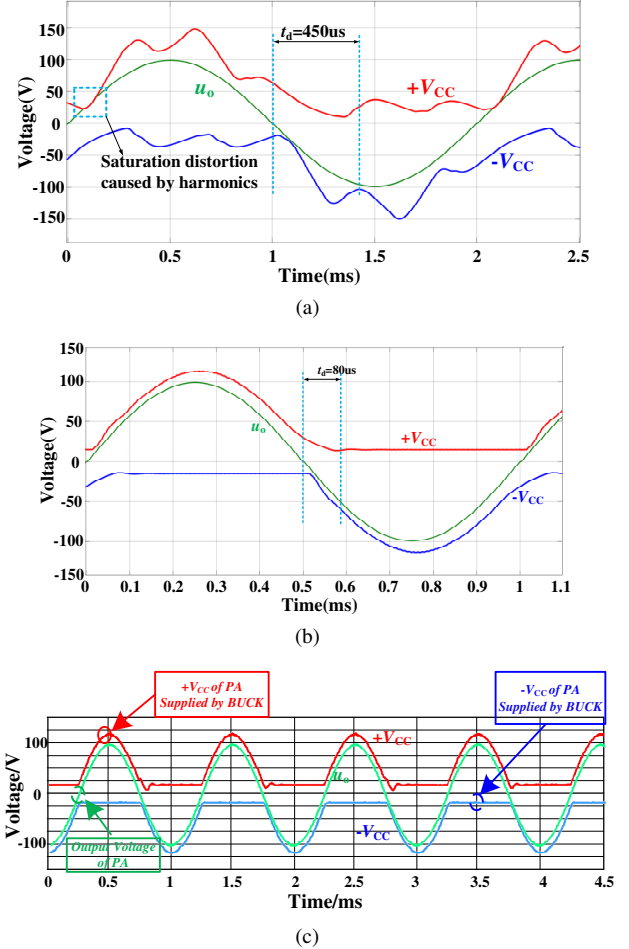
TABLE II
COMPARISON OF PA EFFICIENCY UNDER TWO MODES

U_{om}	PA efficiency under Normal power supply	Under RTSPSs system		
		PA efficiency	BUCK efficiency	Total efficiency
30V	10.7%	85%	80%	68%
50V	19.2%	92%	89%	81.9%
100V	38%	96%	95.5%	91.5%
150V	59.2%	97.2%	96.8%	94.3%
180V	70%	97.8%	97.2%	95%

However, 100kHz is a challenge for the traditional silicon (Si) devices. Thanks to the emerging wide-band-gap devices such as Silicon Carbide (SiC) and Gallium Nitride (GaN), which have high switching-speed and low on-resistance. Hence, the wide-band-gap devices can provide favorable

conditions for realizing the proposed RTSPSs system. Meanwhile, its characteristics are slightly affected by temperature changes. Hence, the SiC MOSFET could maintain the superior performance and reliability of the system for long-time running [19].

When the bus voltage is ±200V, the switching frequency is 100kHz, the output voltage of the PA is 100V, the load resistance is 20Ω and the u_{CES} is set as 5V, the efficiency of the PA under other working conditions is shown in Table II. It obviously manifests that the proposed RTSPSs system can effectively improve the efficiency of the power amplifier compared with the traditional power supply mode.

D. Loss model of RTSPSs System

In order to clarify the overall power losses of the power circuit, the loss of the single BUCK converter is analyzed in consideration of the symmetry of the proposed RTSPSs system. The losses are mainly generated by the switching devices, freewheeling diode, inductor and capacitor. The positive direction of voltage and current on each device is as shown in Fig. 13. Ideally, the voltage and current waveforms of each device in a switching process are shown in Fig. 14.

According to Fig. 14, the conduction losses, turn-on losses, and turn-off losses of the switching device are calculated as follows:

$$P_{S\_con} = i_{DS}^2 \cdot R_{DS(on)} = I_L^2 \cdot R_{DS(on)} \quad (14)$$

$$P_{S\_on} = f_{SW} \cdot \left[V_{DC} \cdot \int_{t_1}^{t_2} i_{DS}(t)dt + I_L \cdot \int_{t_2}^{t_3} u_{DS}(t)dt \right] \quad (15)$$

$$\approx \frac{1}{2} f_{SW} \cdot V_{DC} \cdot I_L \cdot (t_3 - t_2) \approx \frac{1}{2} f_{SW} \cdot V_{DC} \cdot I_L \cdot t_r$$

$$P_{S\_off} = f_{SW} \cdot \left[I_L \cdot \int_{t_6}^{t_7} u_{DS}(t)dt + V_{DC} \cdot \int_{t_7}^{t_8} i_{DS}(t)dt \right] \quad (16)$$

$$\approx \frac{1}{2} f_{SW} \cdot V_{DC} \cdot I_L \cdot (t_7 - t_6) \approx \frac{1}{2} f_{SW} \cdot V_{DC} \cdot I_L \cdot t_f$$

The conduction loss, turn-on loss, and turn-off loss of the freewheeling diode are calculated as follows:

$$P_{D\_con} = I_L \cdot V_F \quad (17)$$

$$P_{D\_on} = f_{SW} \cdot \int_{t_6}^{t_7} u_{DS}(t) i_{DS}(t)dt$$

$$= \frac{1}{6} f_{SW} \cdot I_L \cdot (V_F + V_R) \cdot (t_7 - t_6) \quad (18)$$

$$\approx \frac{1}{6} f_{SW} \cdot I_L \cdot (V_F + V_{DC} - I_L \cdot R_{DS(on)}) \cdot t_f$$

$$P_{D\_off} = f_{SW} \cdot \left[V_F \cdot \int_{t_1}^{t_2} i_D(t)dt + \int_{t_2}^{t_3} i_D(t) u_D(t)dt \right]$$

$$= \frac{1}{2} f_{SW} \cdot V_F \cdot (I_L + I_{RM}) \cdot (t_2 - t_1) + \frac{1}{6} f_{SW} \cdot V_R \cdot I_{RM} \cdot (t_3 - t_2) \quad (19)$$

$$\approx \frac{1}{2} f_{SW} \cdot V_F \cdot (I_L + I_{RM}) \cdot \frac{1}{2} t_{rr} + \frac{1}{6} f_{SW} \cdot (V_{DC} - I_L \cdot R_{DS(on)}) \cdot I_{RM} \cdot t_r$$

$$= \frac{1}{4} f_{SW} \cdot V_F \cdot (I_L + I_{RM}) \cdot t_{rr} + \frac{1}{6} f_{SW} \cdot (V_{DC} - I_L \cdot R_{DS(on)}) \cdot I_{RM} \cdot t_r$$
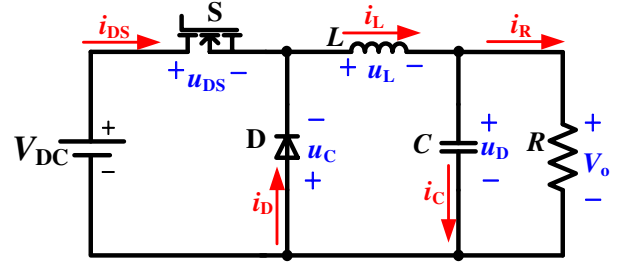

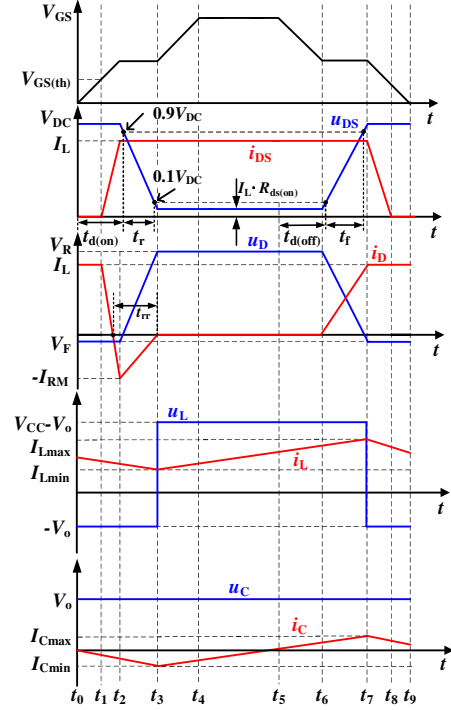Fig. 13. The positive direction of voltage and current on each device.

Fig. 14. The voltage and current waveforms of each device.

where, f_{SW} is the switching frequency, $R_{DS(on)}$ is the on-resistance of the switching device, V_{DC} is the bus voltage, I_L is the current through the inductor, t_r and t_f are the rise time and fall time of the switching device respectively, V_F and V_R are the forward voltage drop and reverse cut-off voltage of the freewheeling diode respectively, I_{RM} and t_{rr} are the maximum reverse recovery current and reverse recovery time of the freewheeling diode respectively.

The losses of the inductance and capacitance can be calculated as follows:

$$P_{Cu} = I_L^2 \cdot R_L \quad (20)$$

$$P_C = I_C^2 \cdot R_C \quad (21)$$

where R_L and R_C are the equivalent resistances of inductances and capacitances respectively.

When the bus voltage is ±200V, the switching frequency is 100kHz, the output voltage of the PA is 100V, the load resistance is 20Ω and the u_{CES} is set as 5V, then the output power and the efficiency of each level are shown in Fig. 15. If

TABLE III
EFFICIENCY COMPARISON BETWEEN CALCULATION AND SIMULATION

U_{om}	Under Normal power supply		Under RTSPSs system	
	Calculation	Simulation	Calculation	Simulation
30V	11.78%	10.7%	86.49%	85%
50V	19.63%	19.2%	92.70%	92%
100V	39.25%	38%	96.4%	96%
150V	58.88%	59.2%	97.93%	97.2%
180V	70.65%	70%	98.58%	97.8%

the normal power supply mode is used, the output power and

the efficiency of the PA are shown in Fig. 16.

It can be seen from Fig. 16(b) that under the same working conditions, the efficiency of the PA is increased from 38% to 96% by using the proposed RTSPSs system. The efficiency of the PA under other working conditions is shown in Table II. The results clearly demonstrate that the proposed RTSPSs system can effectively improve the efficiency of the power amplifier compared with the traditional power supply mode. The simulation results are basically consistent with the calculation results by the established loss model of PA as shown in Table III.

III. PMSM DRIVE SYSTEM BASED ON PAS

A. Circuit topology and control logic

PMSM drive control, a PMSM drive topology based on PAs and the RTSPSs is proposed shown in Fig. 17.

The topology has three closed-loop controls: voltage closed-loop, current closed-loop, and speed closed-loop. The voltage closed-loop is used to keep the output voltage of the RTSPSs following the sinusoidal output voltage of PAs to improve the efficiency without the distortion of the output voltage. The rotor position signal of the motor detected by the resolver and the phase current detected by current sensors are transmitted to the controller to complete the calculation of the speed loop

are used as the input signal of the PAs after D/A conversion and isolation.

The control structure block diagram of the PA drive system is shown in Fig. 18. After the given speed signal *spd** is compared with the actual speed *spd* of PMSM detected by the resolver, the speed-loop PI is adjusted to obtain the given q-axis current signal i^*_q. Meanwhile, the phase currents i_a、 i_b、 i_c, and the angular speed signals ω are converted to the actual

(a)

(b)
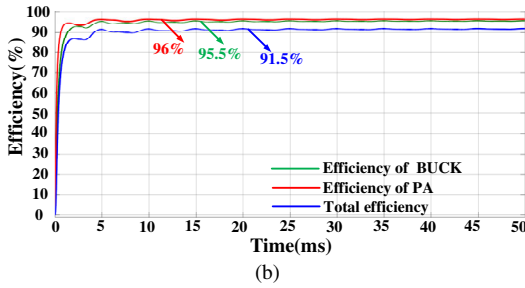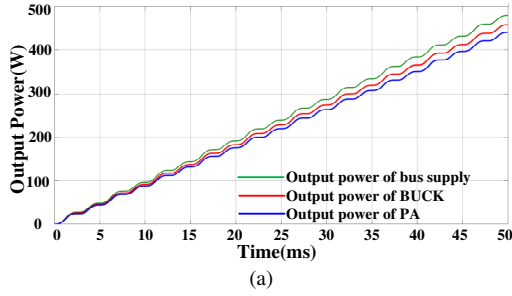
Fig. 15. Under RTSPSs model. (a) Output power of each stage. (b) Efficiency of each level.

(a)

(b)
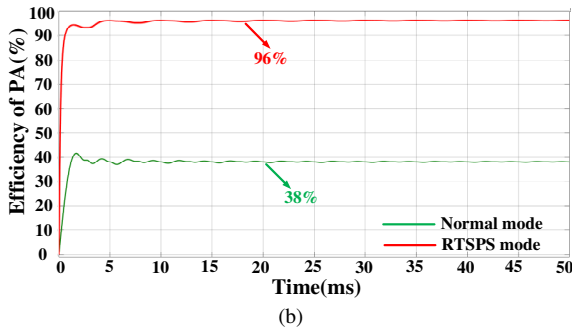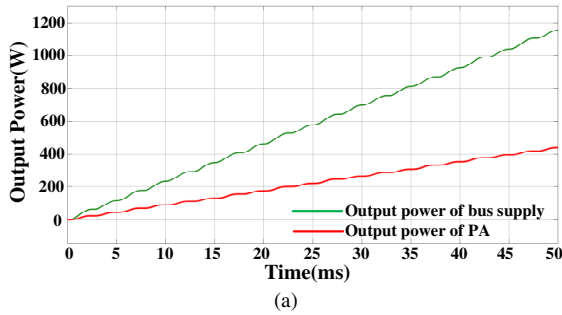
Fig. 16. Output power and efficiency comparison of PAs under normal power supply model. (a) Output power of each stage. (b) Comparison of PA efficiency under two models.

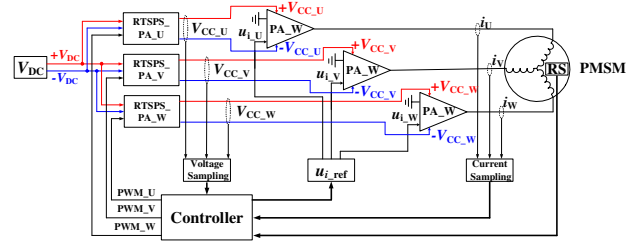and current loop. Then the three-phase voltage control signals

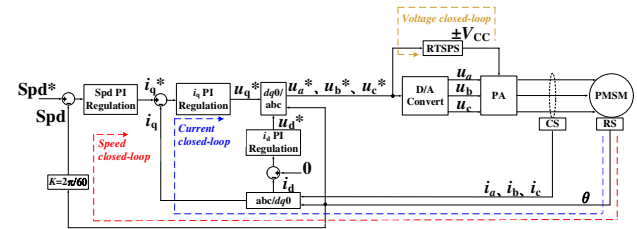Fig. 17. The PMSM drive topology based on PAs and the RTSPSs.

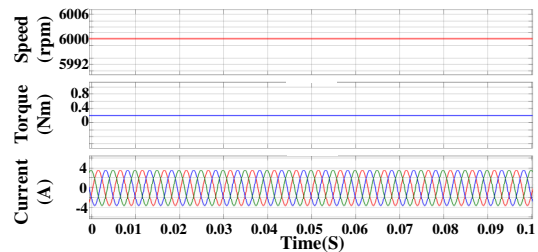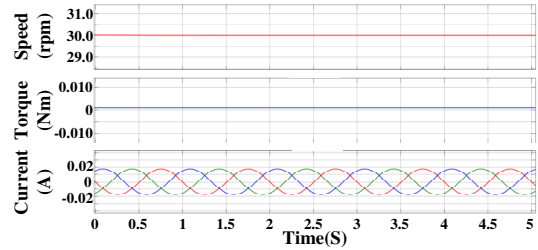Fig. 18. The control structure block diagram of the motor drive system based on PAs and RTSPSs.

(a)

(b)

Fig. 19. Simulation results with PA drive system. (a) 30rpm. (b) 6000rpm.

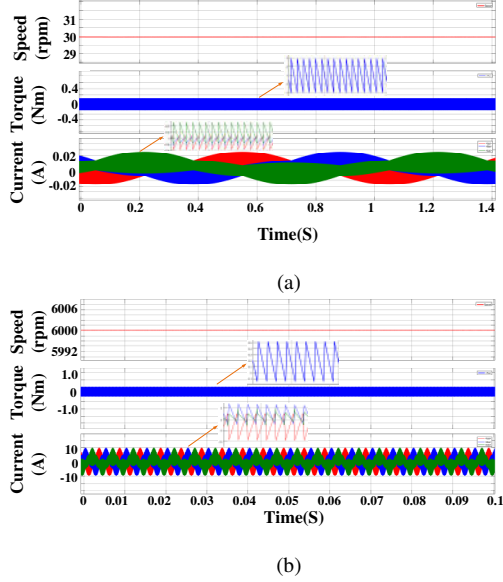q-axis current signal i_q and d-axis current signal i_d by Clarke

(a)

(b)

Fig. 20. Simulation results with SVPWM drive system. (a) 30rpm. (b) 6000rpm.

TABLE IV
Comparison of current harmonics and torque ripple at different loads under two modes

Speed	Torque	Based on PAs		Based on SVPWM	
		THD of current	Torque ripple	THD of current	Torque ripple
30rpm	0.1 N·m	0.02%	0~+0.001	29.73%	-0.1~+0.1
	1 N·m	0.03%	0~+0.005	21.3%	-0.5~+0.2
	10 N·m	0.06%	0~+0.006	5.6%	-0.5~+1.8
6000rpm	0.1 N·m	0.02%	0~+0.2	35.3%	-0.1~+0.4
	1 N·m	0.04%	0~+0.2	17.10%	-0.1~+0.8
	10 N·m	0.09%	0~+0.2	2.61%	-0.1~+0.5

transform and Park transform. Then, the difference between i_q^* and i_q is calculated by the q-axis current PI, and the difference between 0 and i_d is calculated by the d-axis current PI to obtain the given voltage signal u_q^* and u_d^*, respectively. Then, the given three-phase voltage values u_a^*、 u_b^* 、 u_c^* are obtained through inverse Park transformation and inverse Clarke transformation. Meanwhile, u_a^*、 u_b^* 、 u_c^* are also used as given values for the RTSPSs to generate a sinusoidal power supply voltage. Then, the voltages u_a^*、 u_b^* 、 u_c^* are amplified to U_a、 U_b、 U_c to drive the PMSM through D/A conversion and power amplification.

B. Simulation of the proposed drive system

The simulation was carried out in Simulink based on Fig. 18, and the simulation results under low speed and light load are shown in Fig. 19. For the traditional SVPWM, the simulation results with the same motor and working conditions are shown in Fig. 20.

The total harmonic distortion (THD) of the phase current waveform can be obtained by Fourier analysis. The comparison results of the current harmonics and torque ripple of different load are shown in Table IV.

It can be seen from Table IV that the phase current THD and torque ripple in the PMSM drive system based on PAs are much smaller than the drive system based on SVPWM under different loads, especially at low speed and light load. When the speed is 30rpm and the torque is 0.1 Nm, the phase current THD is only 0.02% in the PA drive system, while the current THD is as high as 29.73% in the SVPWM system, the stator current and its THD are shown in Fig. 21(a) and (b). To further prove the advantages of the proposed topology in suppressing harmonics, we can add a filter to the SVPWM inverter, and compare this two circuits. LC filter is selected
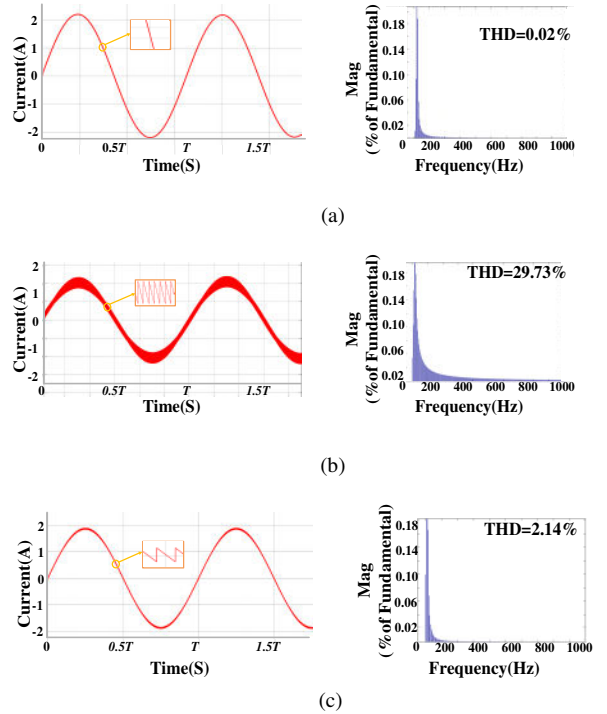

(a)

(b)

(c)

Fig. 21. Stator current and its THD in different mode. (a) PA drive system. (b) SVPWM drive system. (c) SVPWM drive system with filter.

here, and the parameters are set as L_f=174μF, C_f=6.825μF. When the filter is added to the system, the THD becomes 2.14%, as shown in Fig. 21(c). By comparing Fig. 21(a) and Fig. 22(c), the filtering effect of phase current harmonic by using inverter with filter is still not as obvious as the proposed topology.

It can be inferred that the PMSM drive system with PAs can achieve high-precision, especially under conditions of low speed and light load, and reduce the additional losses of motor caused by current harmonics.
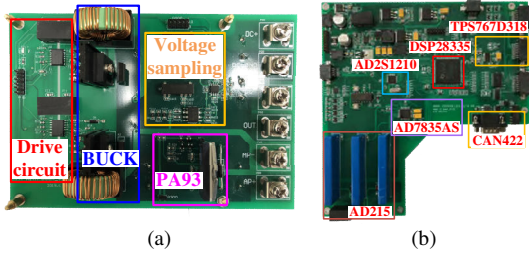
(a)   (b)

Fig. 22. The designed PCB. (a) RTSPSs PCB. (b) Controller PCB based on DSP28335.
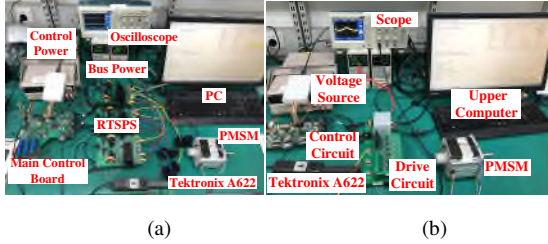

(a)   (b)

Fig. 23. The PMSM drive experimental platform. (a) Based on PAs and RTSPSs. (b) Based on traditional SVPWM.

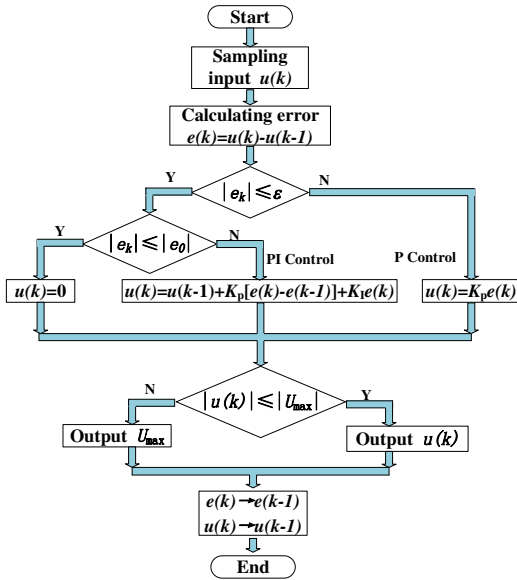
Fig. 24. Flow chart of PI regulator algorithm.

IV. EXPERIMENT AND ANALYSIS

A prototype was designed and manufactured, which includes a controller board based on DSP28335 and three driver boards based on PAs and RTSPSs as shown in Fig. 22. The PMSM drive experimental platform based on both PAs and traditional SVPWM are set up as shown in Fig. 23(a) and (b) respectively.
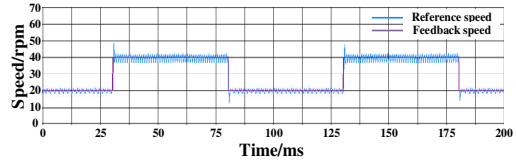
From Fig. 23(a), the current sensor used in the closed-loop control of the drive system is the Hall-type current sensor DHAB S/14 produced by LEM, and the high-precision voltage
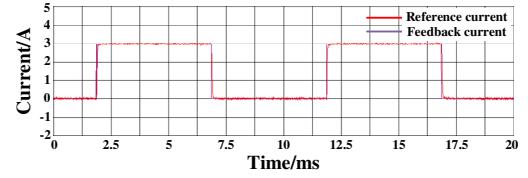
(a)
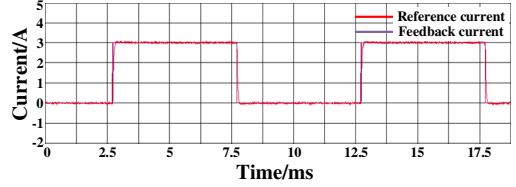
(b)

(c)

Fig. 25. PI regulation following results. (a) Straight axis current following results. (b) Quadrature axis following results. (c) Speed

probe P5100A is used to detect the output voltage of the PA. The current clamp Tektronix A622 can accurately observe the motor phase current waveform. The motor is a 4-pair permanent magnet synchronous motor and the resolver is produced by Tamagawa.

The motor drive experimental platform based on the SVPWM in Fig. 23(b) adopts the same motor, resolver, current clamp and voltage probe as the PA drive platform. The control board is still based on the DSP28335 and the power devices are SiC MOSFET C2M0025120D (1200V/90A) produced by CREE with an on-resistance of 25mΩ. The current sensor uses the on-chip type CKSR 75-NP produced by LEM.

Based on the experimental platform shown in Fig. 23 and the separated PI adjustment algorithm with limiters shown in Fig. 24, experimental comparisons are conducted between the PA-based drive system and SVPWM motor drive system. It should be noted that the switching frequency of the MOSFET is 100kHz and the saturation voltage drop U_{CE} is set to 15V in the PA-based motor drive system, while the switching frequency of the inverter is 15kHz and the dead time is set to 1 μs in SVPWM drive system. And the bus voltage value is 60 VDC.

The given current is set as a square wave with 100Hz frequency and the amplitude of 0A to 3A. The following results under the PI adjustment of the d-axis current i_d and the PI adjustment of the q-axis current i_q are shown in Fig. 25(a) and (b). As shown in Fig. 25(c), the given speed is set to a square wave with 10 Hz frequency and amplitude of 20rpm to 40 rpm.

TABLE V
Comparison of speed ripple under different given speed

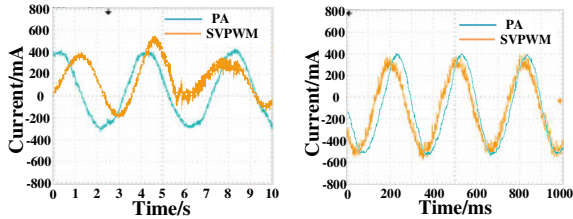| Given speed	Based on PAs and RTSPSs		Based on SVPWM	
	Maximum speed ripple	Error	Maximum speed ripple	Error
2rpm	0.5rpm	25%	27 rpm	1350%
50rpm	4rpm	8%	12 rpm	24%
500rpm	2 rpm	0.4%	8 rpm	1.6%
1000rpm	4 rpm	0.4%	6 rpm	0.6%
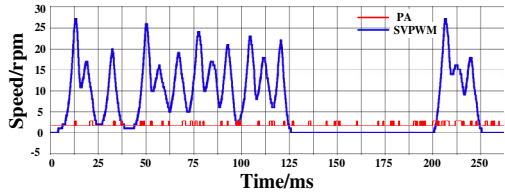
(a)
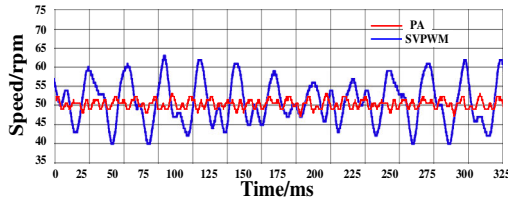
(b)

Fig. 26. Comparison of speed ripple. (a) 2rpm. (b) 50 rpm.


(a)   (b)

Fig. 27. Comparison of current harmonic under different speed. (a) 2rpm. (b) 50rpm.

Fig. 25 shows that the current fluctuation is less than 1mA, and the speed fluctuation is less than 5rpm based on PAs and designed PI regulation.

In the two control modes, a comparison experiment is performed on the speed ripple and phase current harmonics of the motor under two control modes. The experimental results are shown in Fig. 26 and Fig. 27.
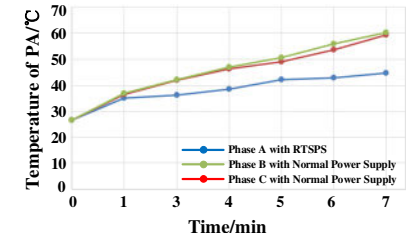
From the comparison shown in Fig. 26, the speed ripple in the PAs-based PMSM drive system is less than that based on the traditional SVPWM system under the same given speed. Especially at 2rpm given speed in Fig. 26(a), the drive system
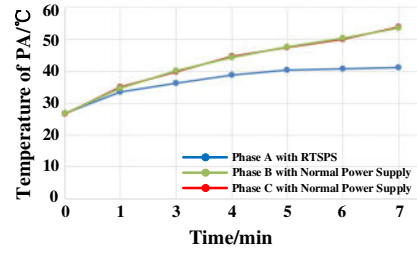
(a)
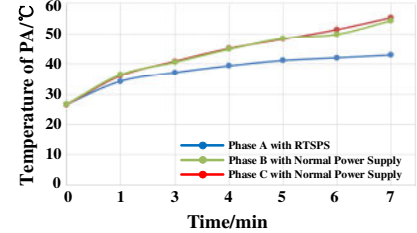
(b)

(c)

Fig. 28. Comparison of PA temperature rise. (a) 400rpm. (b) 800 rpm. (c) 1500 rpm.
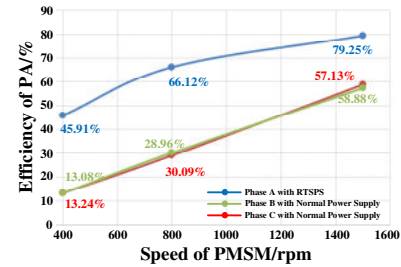

Fig. 29. Comparison of PA efficiency with different speeds.

can still keep the motor running smoothly based on PAs, while the speed of the motor has shown a "crawling" state in the SVPWM drive system, which demonstrates an excellent performance on high-precision control of the PA drive system. The different speed ripples are compared in Table V.

From the comparison of the motor phase currents at different speeds shown in Fig. 27, the phase currents harmonics of the motor in the PAs-based PMSM drive system are significantly smaller than that in traditional SVPWM drive system. When the peak value of phase current is only 400mA, the current in PA drive system is still a sinusoidal waveform, hence, the accuracy of the motor speed is higher. At the same time, the phase current is significantly distorted during the

zero-crossing stage due to the dead time, which causes serious speed ripple and losses of motor in SVPWM drive system.

In order to further verify the effectiveness of the proposed RTSPSs in improving the efficiency of the PAs in the motor drive system, a comparative experiment is also performed. The power supply of phase A is under the RTSPSs, while phase B and C are under the traditional constant voltage power supply. The temperature of the three-phase PAs is detected by a laser thermometer. The bus voltage is ±60VDC and the saturation voltage drop of the PA is set to 15V, and the motor runs at 400rpm, 800rpm, and 1500rpm, respectively. With the running time, the temperature change of each phase linear power amplifier is shown in Fig. 28.

Both Fig. 28 and Fig. 29 manifest the RTSPSs can effectively reduce the temperature rise of the PA. The maximum temperature difference can reach 16℃, and the PA efficiency has increased from 58.88% to 79.25%. And the proposed RTSPSs can significantly improve the PA efficiency at the full speed range of the motor. In addition, if PA93 works at the maximum voltage, namely ± 200VDC, the speed range of the motor is expected to be extended accordingly, and the average output efficiency of the controller should be higher.

V. CONCLUSION

This paper demonstrates a novel PMSM drive system based on linear PAs and RTSPSs, which have the advantages of high linearity and small ripple. The proposed RTSPSs is based on wide-band-gap devices and BUCK converters, which improves the conversion efficiency of PAs without output voltage distortion distinctly. Experiment results show that the PA efficiency is increased from the conventional 58.88% to 79.25%, and the temperature is reduced by 16℃, which also improves the reliability of the PAs and relaxes the limitations of the applied occasion. Compared with the traditional SVPWM drive system, the proposed drive system can achieve high-precision control of the motor, especially at low speed and light load. Hence, the proposed drive system realizes a motor-friendly drive control with high precision and high efficiency.

REFERENCES

[1] Ding, Xiaofeng , et al. "Analytical and Experimental Evaluation of SiC-inverter Nonlinearities for Traction Drives Used in Eletric Vehicles." *IEEE Transactions on Vehicular Technology* PP.99(2017):1-1.

[2] Liang, Wenyi, Luk, Patrick, Fei, Weizhong, "Investigation of Magnetic Field Interharmonics and Sideband Vibration in the FSCW IPMSM Drive With the SPWM Technique," Power Electronics, IEEE Transactions on 33.4(2018):p.3315-3324.

[3] Huang, Wenxin , Hu, Yuwen , and Li, Lei . "Novel Dead-Time Compensation Strategy for Space Voltage Vector PWM Inverter." *Transactions of Nanjing University of Aeronautics & Astronautics* 2:143-147.

[4] Li, Xinjun , and Wu, Tiebin . "Dead-time Compensation Strategy Based on SVPWM." *TheWorld of Inverters* 05(2010):78-81.

[5] Lin, Yong Kai , and Y. S. Lai . "Dead-Time Elimination of PWM-Controlled Inverter/Converter Without Separate Power Sources for Current Polarity Detection Circuit." *IEEE Transactions on Industrial Electronics* 56.6(2009):2121-2127.

[6] Wu, Maogang , Zhao, Rongxiang , and Tang, Xinzhou . " Analysis and compensation method of dead time effectfor for space vector PWM inverter." *Journal of Zhejiang University(Engineering Science)* 26.3(2006):469-473.

[7] Kerkman, R. J. , et al. "Effects of parasitics on the control of voltage source inverters." *IEEE Transactions on Power Electronics* 18(2003):p.140-150.

[8] Bojoi, I R , et al. "Self-commissioning of inverter nonlinear effects in AC drives." *Energy Conference & Exhibition* IEEE, 2012.

[9] Wang, L.Ngai-Man Ho, C.Canales, F.Jatskevich, J. "High-Frequency Modeling of the Long-Cable-Fed Induction Motor Drive System Using TLM Approach for Predicting Overvoltage Transients." *Power Electronics, IEEE Transactions on* 25.10(2010):p.2653-2664.

[10] Bai, Ying , et al. "Design and Realization of Pwm Direct Current Servo System Based on Linear Operational Power Amplifier Module." *Chinese Journal Of Electron Devices* 1(2006):272-274.

[11] Zhou, Wei , et al. " Analysis of Using Power Amplifier to Drive Stepper Motor." *Micromotors* 034.5:33-35.

[12] Wallenhauer, Carsten, et al. "Efficiency-Improved High-Voltage Analog Power Amplifier for Driving Piezoelectric Actuators." *IEEE Transactions on Circuits and Systems I-regular Papers* 57.1 (2010): 291-298.

[13] Kim, Ildu , et al. "High-Efficiency Hybrid EER Transmitter Using Optimized Power Amplifier." *IEEE Transactions on Microwave Theory & Techniques* 56.11(2008):2582-2593.

[14] Helaoui, M , et al. "A New Mode-Multiplexing LINC Architecture to Boost the Efficiency of WiMAX Up-Link Transmitters." *IEEE Transactions on Microwave Theory and Techniques* 55(2007):p.248-253.

[15] Rodriguez, M., et al. "Fast dynamic response multilevel converter for voltage tracking applications." *european conference on power electronics and applications* (2009): 1-10.

[16] Rodriguez, M., et al. "Multiple-input buck converter optimized for accurate envelope tracking in RF power amplifiers." *applied power electronics conference* (2010): 715-722.

[17] Kim, Jooseung, et al. "Envelope-Tracking Two-Stage Power Amplifier With Dual-Mode Supply Modulator for LTE Applications." *IEEE Transactions on Microwave Theory and Techniques* 61.1 (2013): 543-552.

[18] Ding, Xiaofeng, et al. "A Real-time Sinusoidal Voltage-Adjustment Power Supply Based on Wide-Band-Gap Devices for A Linear Power Amplifier." 2019 IEEE Energy Conversion Congress and Exposition (ECCE), Baltimore, MD, USA, 2019, pp. 4043-4049.

[19] Ding, Xiaofeng, et al. "Comprehensive comparison between silicon carbide MOSFETs and silicon IGBTs based traction systems for electric vehicles." Applied Energy (2017): 626-634.